Journal of Materials Research and Technology 27 (2023) 3751–3760

Contents lists available at ScienceDirect

Journal of Materials Research and Technology

journal homepage: www.elsevier.com/locate/jmrt

Review Article

Design and characterization of a novel lightweight multicomponent alloy $Al_{58}Zn_{28}Mg_6Si_8$

J.J. Trujillo-Tadeo [a,*], Gurutze Arruebarrena [a], H.J. Dorantes-Rosales [b], Yoana Bilbao [c], Iban Vicario [d], Teresa Guraya [c], Iñaki Hurtado [a]

[a] Mechanical and Manufacturing Department, Faculty of Engineering, Mondragon Unibertsitatea, 20500 Arrasate/Mondragon, Spain
[b] Instituto Politécnico Nacional, ESIQIE, 07300, CDMX, Mexico
[c] Department of Mining & Metallurgical Engineering and Materials Science, Faculty of Engineering of Bilbao (UPV/EHU), 48013 Bilbao, Spain
[d] Manufacturing Processes and Materials Department, Tecnalia, Basque Research and Technology Alliance (BRTA), 48160 Derio, Spain

ARTICLE INFO

Keywords:
Multicomponent alloys
CALPHAD
Light weight alloys
Spinodal decomposition
Miscibility gap

ABSTRACT

This paper presents a novel multicomponent alloy $Al_{58}Zn_{28}Mg_6Si_8$, with a density of 3.46 g/cm^3, which incorporates concepts from high entropy alloys. The optimum alloy composition was determined using the CALPHAD approach and binary and ternary diagrams. Microstructural and thermal analyses, including scanning electron microscopy, transmission electron microscopy, X-ray diffraction, and differential scanning calorimetry, revealed a complex phase structure consisting of FCC, HCP, and Laves phases, as well as a metastable miscibility gap. The alloy was heat treated, and the microstructure of each condition was evaluated. The solubilized state exhibited a maximum hardness of 250 HV. Transmission electron microscopy results showed that the alloy undergoes spinodal decomposition during the solution treatment. This study provides valuable information for the future design of lightweight multicomponent alloys combining experimental techniques with the CALPHAD approach.

1. Introduction

Developing lightweight materials for application in the transportation and aerospace industry remains a critical challenge. Reducing weight without compromising structural properties and significantly increasing costs is an effective way to reduce fuel consumption and greenhouse gas emissions [1]. Lightweight materials such as aluminum, magnesium, titanium, and beryllium alloys, which have a density between 1.74 and 4.43 g/cm^3, are commonly used in industry [2]. However, the limited properties and/or manufacturing cost of some of these materials has made it necessary for researchers to develop new alloys that more effectively meet lightweighting requirements.

Multicomponent alloys are currently receiving a lot of attention due to their appealing properties. These alloys are composed of multiple elements with a substantial atomic fraction in their chemical composition. In the last decade, these types of alloys have been given various designations, such as high entropy alloys (HEAs), complex composition alloys (CCAs), and multi-principal element alloys (MPEAs), among others. However, despite the different designations, these alloys share a common characteristic: they explore the central region of multicomponent phase diagrams and are recognized for their excellent combination of properties, such as high strength, ductility, superconductivity, high catalytic activity, corrosion resistance, and radiation tolerance [3–5].

Furthermore, a new subcategory of multicomponent alloys, known as lightweight multicomponent alloys has been developed. These alloys incorporate light metallic elements to reduce weight while maintaining the exceptional mechanical properties mentioned earlier [1,2,6]. The exceptional properties of these alloys are attributed to the high entropy effect, which promotes the formation of solid-solution phases, such as BCC, FCC, and HCP, rather than complex intermetallic phases [7]. However, achieving solid-solution phases remains a complex issue, and the majority of presently developed HEAs also exhibit the formation of intermetallics (or second phases) [8]. Nonetheless, incorporating second phases has also been found to be highly effective in strengthening alloys [9]. In fact, some researchers have proposed a shift in focus from solid-solution alloys to multicomponent alloys that contain intermetallics [10]. These studies have shown that the careful design of these second phases simultaneously promote high strength and good

* Corresponding author.
E-mail addresses: jjtrujillo@mondragon.edu (J.J. Trujillo-Tadeo), garruebarrena@mondragon.edu (G. Arruebarrena), hectordorantes@yahoo.com (H.J. Dorantes-Rosales), yoana.bilbao@ehu.eus (Y. Bilbao), iban.vicario@tecnalia.com (I. Vicario), teresa.guraya@ehu.eus (T. Guraya), ihurtado@mondragon.edu (I. Hurtado).

https://doi.org/10.1016/j.jmrt.2023.10.102
Received 14 July 2023; Accepted 10 October 2023
Available online 14 October 2023

ductility in multicomponent alloys [11].

The formation of solid-solution phases is predicted using criteria based on thermodynamic parameters and rules and utilizing methodologies such as CALculation of PHase Diagrams (CALPHAD), ab-initio models, Molecular Dynamics (MD), Density Functional Theory (DFT), and Artificial Neural Networks (ANN) [8,12–16]. To date, the CALPHAD method could be considered the most direct approach for designing lightweight multicomponent alloys [17]. The most important advantage of the CALPHAD method is that it predicts the higher-order phase diagrams via extrapolation from its constituent lower-order systems, such as binary and ternary systems [18].

Research groups around the world have contributed to the design of multicomponent alloys with a density of less than 4 g/cm^3 and high hardness. In the majority of cases, however, these alloys tend to be too brittle. Li et al. [19] developed the $Mg_x(MnAlZnCu)_{100-x}$ multicomponent alloy by induction melting. These alloys are composed mainly of the HCP phase and Al–Mn icosahedral quasicrystal phases with a density 2.20 g/cm^3 and hardness of 178 HV. Chauhan et al. [20] used mechanical alloying (MA) to design the lightweight $Al_{35}Cr_{14}Mg_6Ti_{35}V_{10}$ multicomponent alloy with a density of 4.05 g/cm^3. The alloy reported a hardness of 460 HV and the final microstructure is composed of one HCP and two BCC phases. Youssef et al. [21] developed $Al_{20}Li_{20}Mg_{10}Sc_{20}Ti_{30}$ using thermodynamic parameters and rules, to obtain a hardness of 622 HV and a density of 2.67 g/cm^3. The alloy was fabricated by MA, obtaining a single-phase FCC during ball milling and transforming to single-phase HCP after annealing. Sanchez et al. [22] used the CALPHAD method to design the $Al_{65}Cu_5Cr_5Si_{15}Mn_5Ti_5$ multicomponent alloy produced via large-scale vacuum die casting. The resulting microstructure had a mixture of simple and complex phases, with a density of 3.70 g/cm^3 and a hardness of 889 HV. Despite the obvious contributions of these works, there is still ample unknown space in low-density multicomponent phase diagrams to be explored.

Motivated by the aforementioned advances, this paper presents a new multicomponent alloy $Al_{58}Zn_{28}Mg_6Si_8$ that is cost-effective, lightweight, and easy to fabricate. The objective was to obtain a majority solid-solution phase reinforced with intermetallic phases via casting. The CALPHAD approach and binary and ternary diagrams were used to determine the appropriate chemical composition and calculate phase stabilities. The experimental results were compared to thermodynamic simulations of both non-equilibrium and equilibrium phases in the alloy. The knowledge generated by the design and characterization of the $Al_{58}Zn_{28}Mg_6Si_8$ alloy will provide valuable insights for the future design of lightweight multicomponent alloys.

2. CALPHAD approach to design LW-MEA

Despite the potential of the CALPHAD approach for designing multicomponent alloys, several factors need to be considered. In particular, large extrapolations from the thermodynamic models inherent to the method may lead to inaccurate evaluation of Gibbs energy [17]. Gorsse et al. [23] studied the limitations of CALPHAD databases when applied to multicomponent alloys. Their results showed that the thermodynamic properties of a quaternary alloy can be correctly predicted by direct extrapolation from the fully evaluated binary systems.

In this work, the principal elements were selected based on their low density, low melting point, stability, compatibility, and fabrication feasibility via the casting process. Expensive or scarce elements were discarded from the selection. The CALPHAD approach was then applied as a design strategy to determine the concentration of each element, phase stabilities, and heat treatment schedules. The major driver of the alloy design was to reduce the density by increasing the molar % of Al, to obtain an Al-based multicomponent alloy [22].

In line with this design strategy, the target in the simulations was set to identify systems that have relatively large (Al) FCC regions. The main assumption in the calculations was that a higher-order system could have a wide range of FCC only if its sub-systems have relatively large FCC regions [24]. Thus, the initial calculations were performed with binary systems; all possible Al-X binaries from the previously selected alloying elements (X is the alloying element) were examined, and those with the largest FCC solubility range were selected. The same calculation was performed with the ternary and quaternary systems. In accordance with the FCC solubility range, one or more systems were selected from each ternary, quaternary, and quinary system as candidate Al-based lightweight multicomponent alloy. The selected elements that met the previous requirements were Zn and Mg. Although silicon has low solid solubility in the aluminum phase (a maximum of 1.59 at. %), it is the primary element that imparts high fluidity and low shrinkage to aluminum alloys [25]. As a result, silicon is beneficial for improving castability and weldability, and therefore it was also selected. The target composition was determined based on the above considerations, which resulted in $Al_{58}Zn_{28}Mg_6Si_8$ (at.%) as the alloy under study.

3. Materials and methods

Thermodynamic calculations were carried out using FactSage software with its Ftlite (2020) light alloy database to select the optimal composition. The target alloy was prepared by gravity casting.

The raw materials used were Al, Si, and Mg from high-purity, and for Zn, Zamak5 was employed as the master alloy (Zn4Al1Cu mass %). These elements were melted in an alumina crucible inside a resistance furnace with forced convection under an argon atmosphere. This prevented the multicomponent alloy from undergoing oxidation and mold-metal interaction. To reduce the burning loss of Mg, the fusion order of the elements was the following: 1) Al was melted first at a temperature of 750 °C, 2) Si and Zamak5 alloy were added, and the melt was left to homogenize for 15 min, and 3) Mg was added.

For the composition analysis, chips were machined from the as-cast samples and dissolved in pure nitric acid (HNO_3). The analysis was conducted using the Inductively Coupled Plasma (ICP) technique. The cast sample was also subjected to densitometry using the Archimedes method.

A Brucker D8 Advance X-ray diffractometer (XRD) with Cr Kα radiation operating at 35 kV and 45 mA, with a scanning step of 4°/min from 20° to 100° (2θ), was used to identify different phases formed in the samples. The X-ray diffraction patterns were indexed using the PDF-4+ 2021 database from the International Center for Diffraction Data (ICDD).

To study the microstructural features of the specimens, standard metallography techniques were conducted. Scanning Electron Microscopy (SEM) and energy-dispersive X-ray spectroscopy (EDS) were also performed with an FEI Nova Nano SEM 450 in backscattered electrons (BSEs) and high-contrast mode to analyze the microstructure and determine the semiquantitative local chemical composition.

All cast samples were subjected to heat treatments in an argon atmosphere and quenched in water. The solidus and liquidus temperatures were estimated using the tangent method, based on data obtained from differential scanning calorimetry (DSC) measurements. The heat treatment temperatures were selected based on the DSC results and the simulations from the CALPHAD method (Equilibrium Solidification & Scheil solidification). In addition, a phase transition analysis was conducted using DSC to identify the dissolution and precipitation reactions of the heat-treated samples. NETZSCH STA 449 F3 Jupiter equipment was used to perform the DSC test. All tests were conducted at a heating and cooling rate of 10 K/min, and in a temperature range of 25 °C–750 °C, thus melting the material "in situ". Immediately after heat treatments, microhardness tests were carried out using a Zwick machine with a Vickers indenter. The test load and duration were 5 kg and 10 s, respectively. All hardness tests were repeated twelve times.

Transmission electron microscopy (TEM) was used to investigate microstructure details. TEM specimens were mechanically ground to ~120 μm thickness, from which 3 mm diameter discs were punched. The

discs were electropolished with a two-jet Fischione using an electrolyte mixture of 1/5 $HClO_4$ and 4/5 CH_3OH with $C_3H_8O_3$. The liquid was kept at −50 °C ± 5 °C with CO_2, and the applied voltage and current were 50 V and 100 mA. The TEM observations were carried out in a Jeol 2000 FXII TEM equipped with EDX at 200 kV.

4. Results

4.1. Phase stability simulations by CALPHAD

Thermodynamic calculations of equilibrium and Scheil solidification of the manufactured alloy were conducted as a function of temperature, and the results are shown in Fig. 1. The chemical composition of the alloy was obtained using ICP analysis (see Table 1). The density of the casting alloy was 3.46 g/cm^3.

Table 1
Chemical composition of lightweight multicomponent alloy obtained with ICP.

Alloy		Al	Zn	Mg	Si	Cu	Sr
LW-MEA	[wt%]	Balance	48.40	4.11	5.83	0.43	0.03
	[at%]	Balance	27.93	6.38	7.83	0.26	0.01

Fig. 1a illustrates the equilibrium solidification sequence of the alloy under consideration. The first phase to precipitate is silicon (Si), at approximately 530 °C, followed by the FCC phase of aluminum (Al) and the intermetallic (Mg_2Si), both at 495 °C. At 350 °C, a miscibility gap appears with the A1#1 (Al) and A1#2 (Al) phases. Furthermore, the solid solution phase (Al) is present at its maximum percentage in the temperature range of 350–380 °C during the equilibrium solidification.

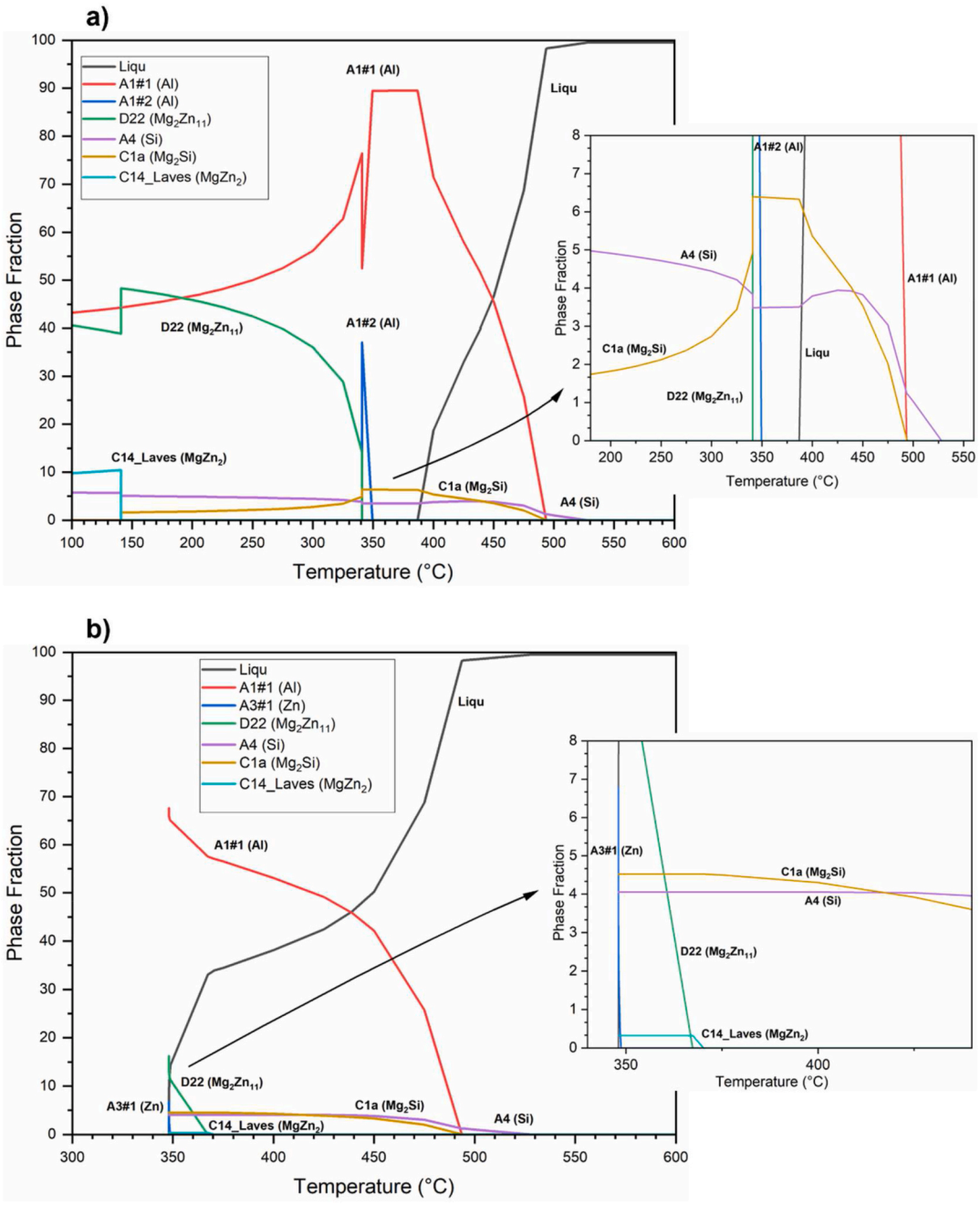

Fig. 1. Solidification simulations for $Al_{58}Zn_{28}Mg_6Si_8$ lightweight multicomponent alloy calculated by FactSage (CALPHAD): a) Equilibrium solidification, and b) non-equilibrium solidification (Gulliver -Scheil).

The precipitation of the (Mg_2Zn_{11}) phase occurs at a temperature of 340 °C. Lastly, the Laves phase ($MgZn_2$) is the last phase to form, appearing at a temperature of 140 °C.

On the other hand, in the non-equilibrium Scheil simulation, the first phase to precipitate is silicon (Si) at a temperature of 530 °C, followed by the (Mg_2Si) and FCC phases of aluminum (Al), which both appear to precipitate at the same temperature of 493 °C. The Laves ($MgZn_2$) phase precipitates at 370 °C, followed by the (Mg_2Zn_{11}) phase, which appears at 367 °C. Finally, at approximately 350 °C, the zinc (Zn) phase precipitates last.

It is worth noting that CALPHAD predicts an important variation in the precipitation order of the ($MgZn_2$) and (Mg_2Zn_{11}) phases. According to Fig. 1b, precipitation begins with the (Mg_2Zn_{11}) phase at 340 °C, and as the temperature decreases towards 140 °C, a partial transformation occurs, leading to the appearance of the Laves ($MgZn_2$) phase. Furthermore, the precipitation of the (Zn) phase is only observed in the Scheil curve. The miscibility gap does not occur in the non-equilibrium simulation.

4.2. Analysis of the microstructure prior to heat treatments

The as-cast $Al_{58}Zn_{28}Mg_6Si_8$ alloy was subjected to an experimental analysis using XRD, DSC, SEM, and EDS techniques. The XRD patterns of the as-cast alloy showed several reflection peaks (Fig. 2) that were successfully indexed to the (Al) phase (PDF: 00-004-0787), ($MgZn_2$) Laves phase (PDF: 04-003-2083), (Mg_2Si) (PDF: 01-083-5235), (Zn) (PDF: 01-078-9363), (Si) (PDF: 00-027-1402), and (Mg_2Zn_{11}) (PDF: 04-007-1412). The phases identified by XRD in the as-cast condition are consistent with those predicted by CALPHAD in the Scheil solidification Fig. 1b.

Fig. 3a displays a backscattered electron image of the as-cast sample, revealing a complex microstructure consisting of dendritic, eutectic, and interdendritic zones with different contrasts can be observed. The dendritic phase (contour A) corresponds to the FCC phase of aluminum (Al), while the interdendritic zone (contour B) may be some of the phases of the Mg–Zn system, either ($MgZn_2$) or (Mg_2Zn_{11}). Contour C corresponds to the eutectic (Al + Mg_2Si), where the gray zone is associated with the (Al) phase, and the darker zones correspond to the (Mg_2Si) phase. While the eutectic (contour D) corresponds to the (Al + Si), with the aluminum phase being the gray zone and the (Si) being the dark gray zone. In addition, Fig. 3a reveals bright regions where heavier elements, such as the zinc (Zn) phase, are located.

The EDS composition analysis shown in Fig. 3d of the dendritic phase

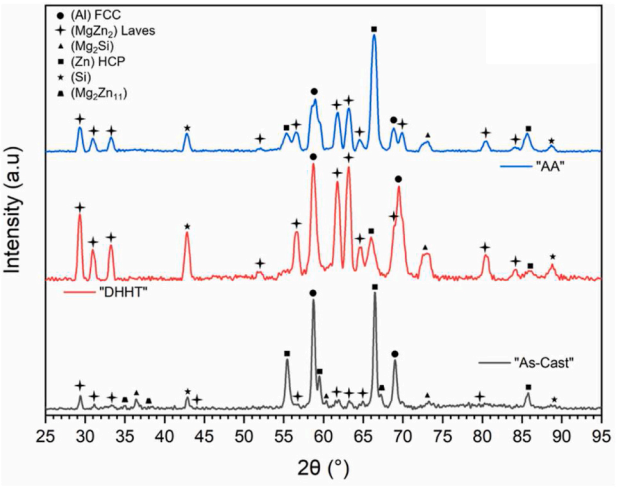

Fig. 2. XRD diffraction patterns for the $Al_{58}Zn_{28}Mg_6Si_8$ lightweight multi-component alloy "as-cast", "DHHT" (Double Homogenization Heat Treatment) and "AA" (Artificial Aging) specimens.

reveals a high concentration of Al (as indicated by points 01), confirming that this phase primarily comprises (Al). The interdendritic zones in the microstructure exhibit variations in their compositions, as indicated by the EDS analysis. For example, point 02 is rich in zinc, followed by magnesium, and based on the atomic composition, corresponds to the laves phase ($MgZn_2$). The varying shades in the interdendritic zones indicate partitioning and segregation between the solid and liquid phases during solidification. The eutectic phase at point 03 has a higher concentration of Mg and Si, which corresponds to the (Mg_2Si) phase. The eutectic structure located at point 04 had a high silicon concentration, estimated to be approximately 97 at.% of silicon, followed by aluminum.

4.3. Design of heat treatments

To optimize the material through heat treatments, it is necessary to determine the critical temperatures at which phase changes or melting of the alloy occur. Simulations using CALPHAD calculate a solidus temperature of 390 °C for equilibrium solidification and a liquidus temperature of 530 °C. For non-equilibrium solidification, the solidus temperature is 350 °C, while the liquidus temperature is 530 °C. However, the differential scanning calorimetry analysis (Fig. 4) reveals that the curve of the heating cycle for the as-cast sample display a solidus temperature of around 400 °C and a liquidus temperature of approximately 580 °C. Indicating that the selected composition has a relatively low melting point and can be easily melted using a standard laboratory furnace.

The heating cycle (Fig. 4) shows the dissolution of seven phases as indicated by the peaks. According to the FactSage results, the highest temperature peak 7 is likely associated with the (Si) phase melting. This is confirmed by the liquid projection of the Al–Si–Zn ternary diagram (Fig. 5), which shows that the phase in question is indeed silicon (Si). In this phase, the solubility of the other alloying elements is close to zero, corresponding to the EDS point 04. The two peaks (peak 6 and peak 5) following silicon (Si) do not appear to be the result of a single-phase transformation, as they show at least two maxima: a peak at about 502 °C (peak 6) and a small peak at about 480 °C (peak 5). Peak 6 is the dendrite (contour A) and peak 5 corresponds to the eutectic (Al + Mg_2Si) (contour D). In addition, peaks 4 and 3 may correspond to the dissolution of ($MgZn_2$) and (Mg_2Zn_{11}) phases, according to the Scheil solidification results (Fig. 1b) and the interdendritic zone (contour B) shown in Fig. 3a. Finally, peak 2 could be attributed to the miscibility gap, as indicated by the equilibrium diagram (Fig. 1a), while peak 1 can be associated with the dissolution of the (Zn) phase according to the Scheil solidification diagram (Fig. 1b).

Based on the analysis mentioned earlier, the heat treatments were prescribed as follows: Initially, solution treatments were carried out in the temperature range of 360–380 °C, which corresponds to the FCC temperature range of equilibrium solidification (as depicted in Fig. 1a), Scheil solidification (Fig. 1b), and DSC results (Fig. 4).

At the beginning of casting, the solidification kinetics of the samples closely resembled the Scheil simulation due to the rapid cooling rate. This can result in variances in the melting temperatures of the samples, which increases the risk of incipient melting during the solution treatment. To mitigate this risk, a two-step solution treatment process was developed and implemented.

In the first step, the material was heated to 325 °C, which is lower than the solidus temperature predicted by FactSage for the Scheil cooling process (Fig. 1b). This temperature of 325 °C was chosen to homogenize the material and prevent incipient melting as the temperature increases. In the second step, the temperature was raised to 380 °C, below the liquidus temperature as indicated by the equilibrium solidification diagram (Fig. 1a). This temperature of 380 °C was selected to dissolve all the secondary phases in the material, as well as to achieve a high percentage of FCC solid solution. The aim was to reach an equilibrium state at this temperature. The sample was then rapidly cooled in

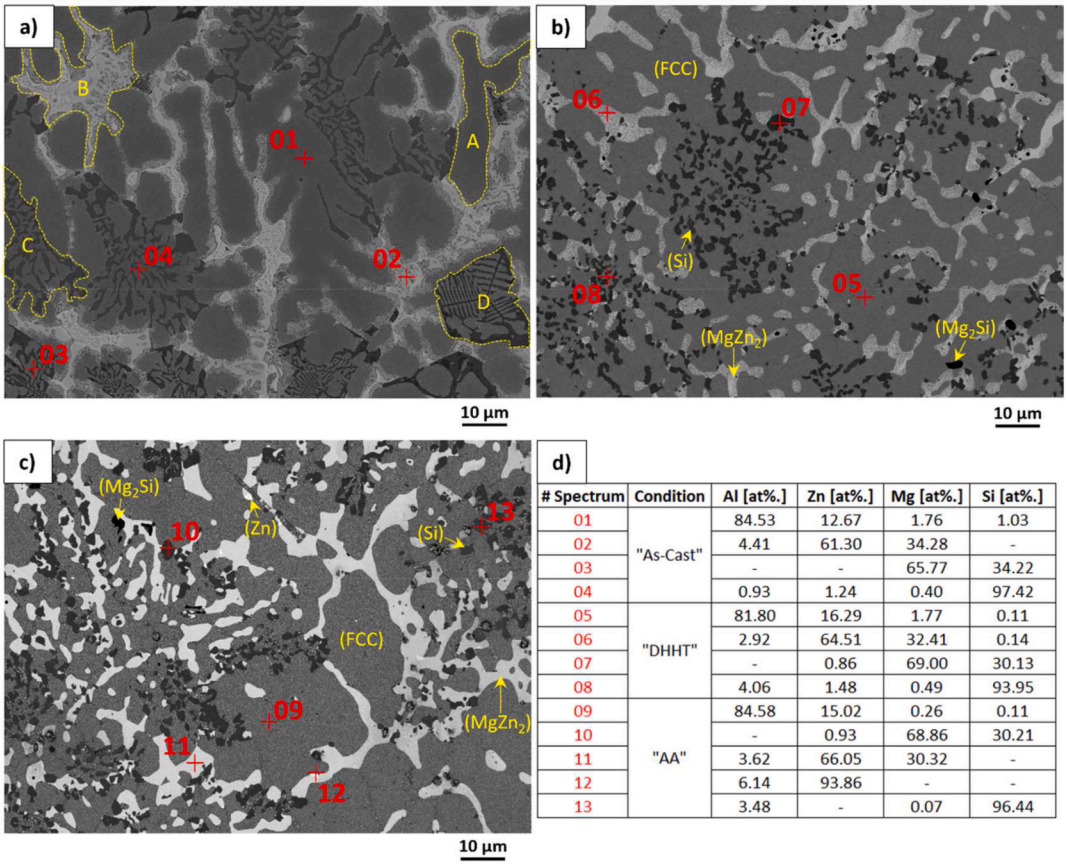

d)

# Spectrum	Condition	Al [at%.]	Zn [at%.]	Mg [at%.]	Si [at%.]
01	"As-Cast"	84.53	12.67	1.76	1.03
02		4.41	61.30	34.28	-
03		-	-	65.77	34.22
04		0.93	1.24	0.40	97.42
05	"DHHT"	81.80	16.29	1.77	0.11
06		2.92	64.51	32.41	0.14
07		-	0.86	69.00	30.13
08		4.06	1.48	0.49	93.95
09	"AA"	84.58	15.02	0.26	0.11
10		-	0.93	68.86	30.21
11		3.62	66.05	30.32	-
12		6.14	93.86	-	-
13		3.48	-	0.07	96.44

Fig. 3. SEM/EDS of the $Al_{58}Zn_{28}Mg_6Si_8$ lightweight multicomponent alloy in condition: a) "As-Cast", b) "DHHT" (Double Homogenization Heat Treatment) and c) "AA" (Artificial Aging).

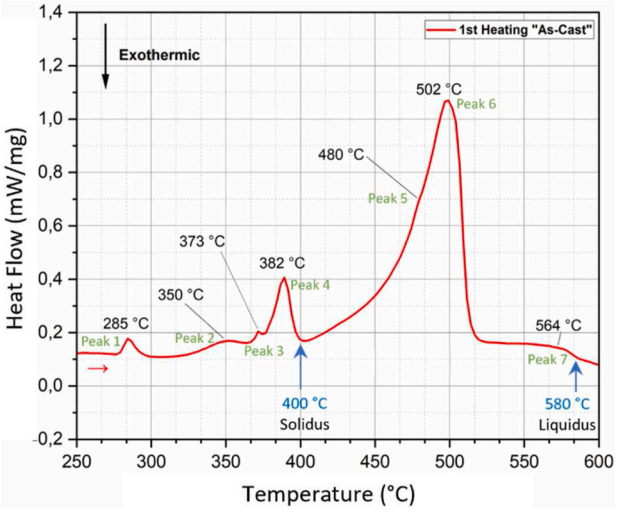

Fig. 4. DSC curve of the $Al_{58}Zn_{28}Mg_6Si_8$ lightweight multicomponent alloy heating process.

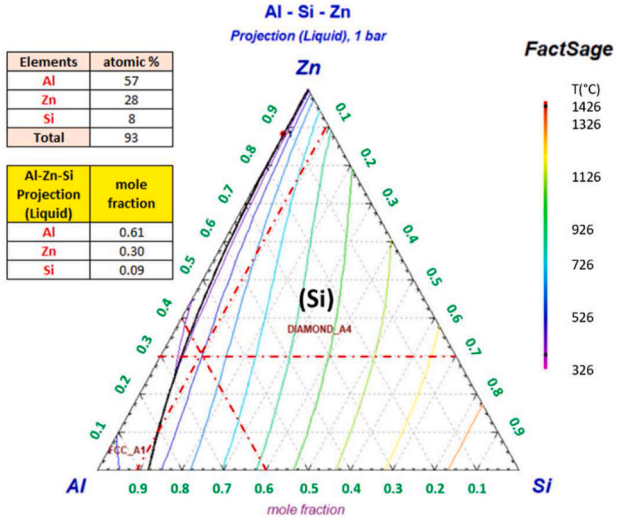

Elements	atomic %
Al	57
Zn	28
Si	8
Total	93

Al-Zn-Si Projection (Liquid)	mole fraction
Al	0.61
Zn	0.30
Si	0.09

Fig. 5. Projection of the liquid on the Al–Si–Zn ternary diagram calculated by FactSage (The intersection of the dotted lines determines the composition of the alloy).

cold water to preserve the structure as much as possible.

Some of the samples were subjected to artificial aging after solution treatment. A temperature of 160 °C and 240 min were selected for the artificial aging process to observe how the phases evolve. Therefore, the samples analyzed in this study correspond to the heat treatment schedules listed in Table 2. The heat treatment labeled DHHT is a double-step solubilization treatment, while the heat treatment marked AA corresponds to artificial aging performed at 160 °C for 240 min.

4.4. *Effect of the heat treatments on the microstructure*

The XRD patterns of the alloy after solubilization treatment show some differences compared to the as-cast alloy, as depicted in Fig. 2. In the double homogenization heat treatment, the (Mg_2Zn_{11}) phase disappears, and the amount of the (Zn) phase is reduced. It is important to

Table 2
Heat treatment schedules for the $Al_{58}Zn_{28}Mg_6Si_8$ lightweight multicomponent alloy.

Sample	Solution Treatment		Artificial Aging after Solutionization
	Step 1	Step 2	
Double Homogenization Heat Treatment "DHHT"	325 °C/24 h	380 °C/24 h + Quenching	–
Artificial Aging "AA"	325 °C/24 h	380 °C/24 h + Quenching	160 °C/240 min

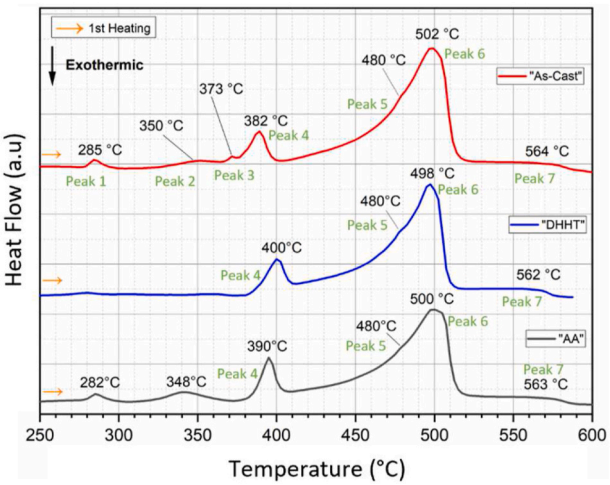

Fig. 6. DSC heating curves for the three conditions, "As-Cast", "DHHT" (Double Homogenization Heat Treatment) and "AA" (Artificial Aging).

note that the sample analysis with the solution treatment was carried out three months after casting. Therefore, it is possible that natural aging occurred, and a small amount of (Zn) precipitated in the matrix. During the artificial aging, the (Mg_2Zn_{11}) phase completely disappears in the diffraction patterns compared to the as-cast sample. Furthermore, during AA heat treatment, the (Zn) phase precipitates again, leading to a noticeable increase in the amount of (Zn) phase compared to the diffraction patterns after the solubilization treatment.

The results of DSC analysis for the heat-treated and non-heat-treated samples are presented in Fig. 6. After conducting DSC analysis on the DHHT sample, the phases corresponding to peaks 2 and 3 were completely dissolved in the matrix due to the dissolution treatment. However, a small amount of the phase corresponding to peak 1 was observed to have precipitated. In the artificially aged sample, it was observed that the phases corresponding to peaks 1 and 2 had precipitated again. Additionally, it was found that the phase corresponding to the dissolution temperature of peak 4 was present in all the curves, irrespective of their heat treatment, with a temperature of approximately 390 °C.

Fig. 3b illustrates a more homogeneous microstructure of the lightweight multicomponent alloy after solution treatment. A mostly FCC matrix with second phases such as ($MgZn_2$), (Si), and (Mg_2Si) can be observed. The ($MgZn_2$) phase appears the brightest, and the (Mg_2Si) phase occurs the darkest. These three intermetallics or second phases are clustered and have formed globular shapes. The presence of these phases is confirmed by the compositional analysis results in Fig. 3d. Point 05 shows a high Al content of around 82 at.%, corresponding to the (Al) phase (FCC). Spectrum 06 confirms the stoichiometry of the ($MgZn_2$) phase, while spectrum 07 corresponds to the chemical composition of (Mg_2Si). Finally, Spectrum 08 indicates a high concentration of silicon, which suggests the presence of the (Si) phase. The backscattered electron image of the artificially aged sample (Fig. 3c) shows a microstructure similar to that in the solubilized condition. However, there are some differences. For example, the matrix in Fig. 3c contains precipitates in its interior. Additionally, brighter zones can be observed, which point to the (Zn) phase, according to the compositional analysis of point 12 (Fig. 3d). This (Zn) phase appears to be located in the interface of the Laves phase ($MgZn_2$), and the matrix (Al) FCC.

4.5. Hardness of samples

The as-cast and heat-treated samples were evaluated for their hardness, and the measured microhardness values are presented in Table 3. The as-cast specimen had a hardness value of HV 184. It can be observed that the solution treatment significantly increases the hardness of the alloy up to a value of 250 HV, while the artificially aged sample shows the lowest microhardness value, with a measurement of 148 HV. This phenomenon may be related to over-aging of the alloy.

5. Discussion

5.1. Phase evolution analysis

Based on the results obtained from CALPHAD, DSC, XRD, and micrographs of the $Al_{58}Zn_{28}Mg_6Si_8$ alloy under different conditions, As-Cast, DHHT (Double Homogenization Heat Treatment), and AA (Artificial Aging). The following sequence of phases that appear during cooling has been proposed. Table 4 displays the transformation temperatures identified from the DSC heating curves.

The precipitation order during solidification is as follows (Fig. 6). Starting with the first phase that forms at high temperature from the liquid, it corresponds to (Si) phase that is supported with the projection of the liquid and the simulation in equilibrium by CALPHAD.

The DSC measurements reveal two additional transition temperatures within the range of 480–500 °C. The peak observed at approximately 500 °C is attributed to the dissolution of the eutectic phase formed by (Al) and (Si). The second peak at 480 °C corresponds to the melting of a eutectic phase formed by (Al) and (Mg_2Si). These two transformations are supported by the microstructures in Fig. 3a, where contour C corresponds to the eutectic formed by (Al) (dark gray) and (Si) (darker zones), and contour D corresponds to the eutectic formed by (Al) (dark gray) and (Mg_2Si) (black). These two phases were further confirmed by EDS measurements (Fig. 3d). Additionally, the precipitation of these two phases agrees with the CALPHAD results.

The fourth phase is associated with the Laves phase ($MgZn_2$). This phase is observed in all the DSC curves (Fig. 6) and all the diffraction patterns (Fig. 2), regardless of the heat treatment at 380 °C. The microstructural and compositional analysis in Fig. 3 validates this intermetallic. It is evident that to dissolve the Laves phase, we must

Table 3
Microhardness of the $Al_{58}Zn_{28}Mg_6Si_8$ lightweight multicomponent alloy.

Alloy	Condition	Microhardness (HV)
Lightweight multicomponent alloy	As-Cast "AC"	184 ± 5
	Double Homogenization Heat Treatment "DHHT"	250 ± 4
	Artificial Aging "AA"	150 ± 2

Table 4
The proposed invariant points of the system $Al_{58}Zn_{28}Mg_6Si_8$ lightweight multicomponent alloy.

Reaction type	Reaction	Temperature (°C)
–	L ↔ (Si)	565
Eutectic	L ↔ (Al) + (Si)	502
Eutectic	L ↔ (Al) + (Mg_2Si)	480
–	L ↔ ($MgZn_2$)	380
Peritectic	L + ($MgZn_2$) ↔ Mg_2Zn_{11}	370
Miscibility gap	(Al)#1 + (Al)#2 ↔ (Al)	350
Eutectoid	(Zn) + (Al)#1 ↔ (Al)#2	280

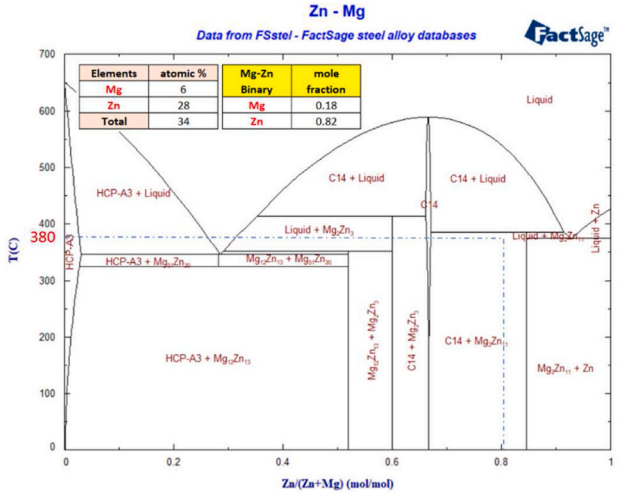

Fig. 7. The Mg–Zn binary phase diagram calculated by FactSage.

increase the temperature of the solubilization above 400 °C, but there is a risk of incipient melting.

The (Mg_2Zn_{11}) is the fifth phase to precipitate and is the only one that appears in the XRD of the As-Cast alloy, which suggests that it could be associated with the small peak at 370 °C that only appears in the DSC curve of the sample in this condition. This phase does not appear in the DHHT and AA samples because the treatment has been above the stability of this phase, at 380 °C. This peritectic reaction, according to Fig. 7 of the Mg–Zn binary phase diagram, has only formed in the As-Cast state due to the higher presence of liquid, which means that it can form a small amount of primary form (the composition of the liquid runs towards higher Zn contents).

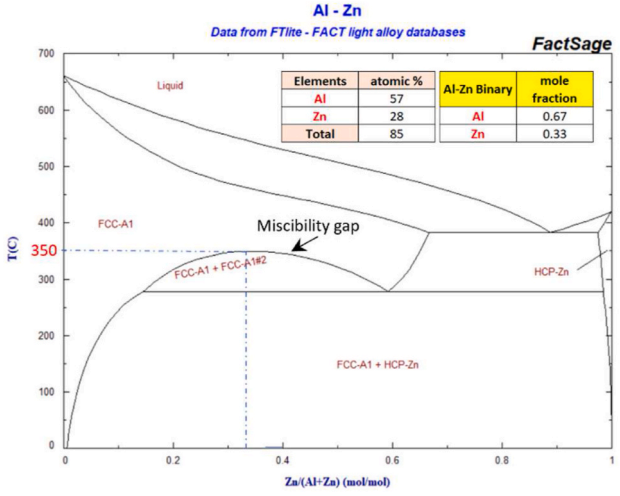

Fig. 8. Binary Al–Zn diagram showing the miscibility gap of the (Al) phase calculated by FactSage.

After equilibrium solidification, a region of immiscibility appears in the (Al) phase, with an (Al)#1 zone containing a low concentration of Zinc and an (Al)#2 zone containing a higher amount of Zn, as shown in Fig. 8 of the Al–Zn binary phase diagram. Kogo et al. [26] conducted a thermodynamic evaluation based on experimental and phase diagram data for the binary Al–Zn system They found a miscibility gap in the FCC-Al phase below the critical temperature of 350 °C. This temperature has been verified to correspond to the second peak of the DSC analysis.

The last phase to precipitate corresponds to (Zn). The XRD results depicted in Fig. 2 reveal that the (Zn) phase precipitates after artificial aging, which is further confirmed by the DSC analysis of the AA sample, as illustrated in Fig. 6. According to the Al–Zn binary phase diagram (Fig. 8), the formation of the (Zn) phase is preferential when (Al)#2 is present in the alloy, and vice versa. The backscattered electron image also confirms this observation, as shown in Fig. 3c. The bright regions correspond to the (Zn) phase. This explains the appearance and disappearance of the two lower temperature peaks in the DSC analysis presented in Fig. 6. The first peak is observed during heating at approximately 280 °C and corresponds to (Zn) + (Al)#1 → (Al)#2, while the second peak, at around 340 °C, corresponds to (Al)#1 + (Al)#2 → (Al).

5.2. Miscibility gap validation and HCP evolution

The kinetics of spinodal decomposition in Al–Zn alloys is extremely rapid, even at low aging temperatures. Studies have shown that the Al-50 % Zn alloy undergoes rapid spinodal decomposition after solution treatment and cooling [27]. To confirm this phenomenon, transmission electron microscopy was employed to examine the microstructure in the solubilized and quenched samples, with the aim of characterizing the phase separation mechanism. The TEM bright field (BF) image and the corresponding selected area electron diffraction pattern (SADP) for the $Al_{58}Zn_{28}Mg_6Si_8$ lightweight multicomponent alloy after double homogenization heat treatment and quenching are shown in Fig. 9. These micrographs verify the formation of a supersaturated solid solution in the alloy after quenching. The TEM image in Fig. 9b shows a modulated microstructure containing a high-volume fraction of second phase. This type of microstructure is typical in alloys that decompose within low temperature miscibility gaps [28].

The SADP shown in Fig. 9c was observed from the zone axis of [013] and indicated a 2.338 Å and 2.024 Å interplanar spacing of the (111) and (200) planes. This is in good agreement with the lattice structure of the (Al) phase FCC with the unit cell parameter of a = 4.0496 Å. In addition, the corresponding electron diffraction pattern showed extra spots (satellites) (Fig. 9c), which are a product of preferential orientation during the spinodal decomposition. Satellite spots can occur because of the presence of planar defects such as stacking faults, line defects such as dislocations, spinodal decomposition, or regular arrays of crystal defects [29].

Similarly, the SADP in Fig. 9d was observed from the zone axis of [$\bar{1}$12], showing interplanar spacings of 3.134 Å, 1.919 Å, and 1.636 Å for the (111), (200), and (311) planes, respectively. These correspond to the diamond cubic crystal structure of the (Si) phase with a unit cell parameter of a = 5.4282 Å. The solution treatment has been shown to increase the strength of the alloy because of the solid solution hardening mechanism, which results from the interaction between dissolved alloying elements and dislocations [24]. The microhardness test results support this observation, with the DHHT sample displaying an increase in hardness of 66 HV compared to the as-cast sample, as shown in Table 3.

In our previous study [30], we investigated the phase evolution of the $Al_{58}Zn_{28}Mg_6Si_8$ alloy as a function of temperature using X-ray Thermo-Diffraction. Our analysis revealed the existence of an additional phase with the same space group as aluminum (Fm3m) but a smaller

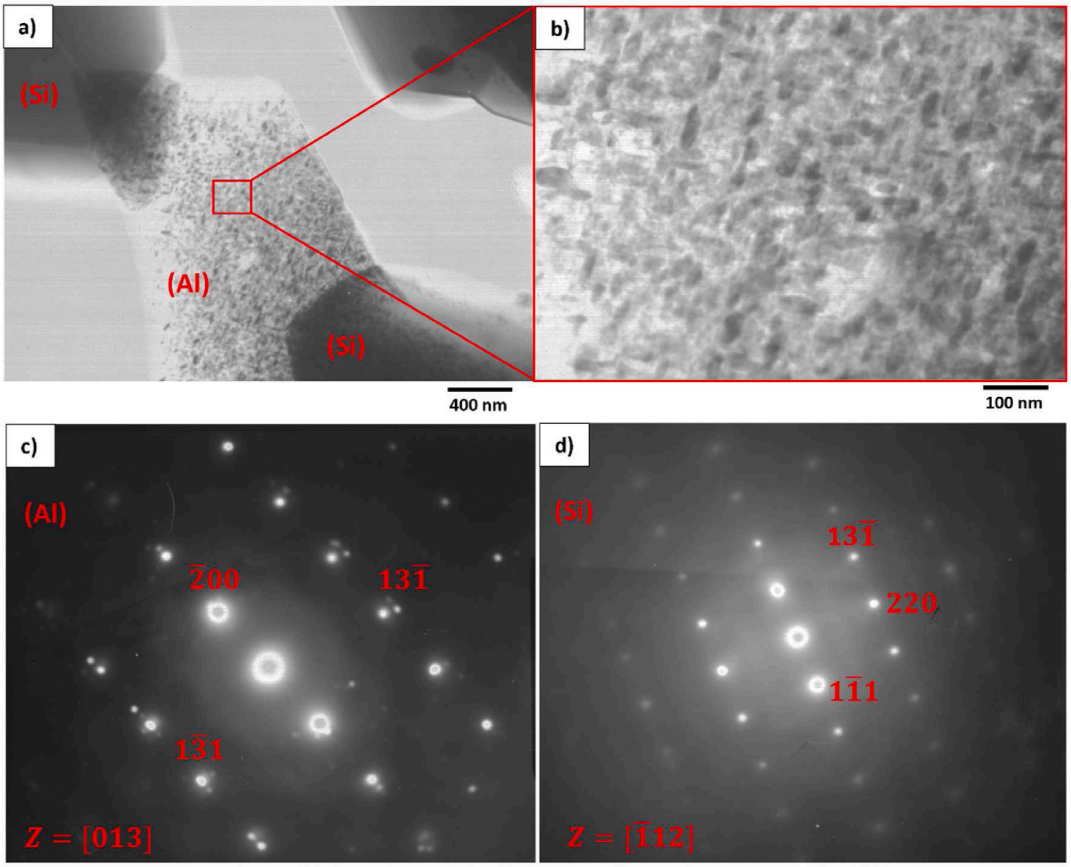

Fig. 9. (a–b) Bright-field TEM micrographs and (c–d) selected area electron diffraction patterns (SADP) confirming the phases in the $Al_{58}Zn_{28}Mg_6Si_8$ lightweight multicomponent alloy after double homogenization heat treatment and quenching, (c) SADP of the (Al) FCC phase and (d) SADP of the (Si) phase.

lattice parameter. Based on our observations, we suggested that this phase could be the (Al)#2 phase of the miscibility gap. Due to the smaller atomic size of zinc compared to aluminum, a zinc-rich aluminum phase have a lower lattice parameter than (Al)#1.

According to Popovic et al. [31], the sequence of precipitation during aging begins with the formation of (Zn-rich) Guinier-Preston zone (GPZ) spheres, with a size of approximately 1–2 nm, that are completely coherent with the Al-rich (Al) phase matrix. Further aging leads to a change in the morphology of GPZ to an ellipsoidal shape that remains coherent with the (Al) phase matrix, with a size of approximately 10 nm. Subsequent aging causes the formation of the metastable Zn-rich (Al)#2 phase. Finally, prolonged aging of this type of alloy obtains the off-equilibrium hexagonal close-packed (HCP) Zn-rich (Zn) phase, which is incoherent with the matrix, as shown in Fig. 10. The XRD and DSC results of the artificially aged alloy, can be attributed to the direct precipitation of (Zn) from the quenched (Al) phase. Upon heating, the second variant of (Al), denoted as (Al)#2, forms at the transformation temperature around 280 °C (peak 1), and the end of the miscibility zone is observed with the second peak at 350 °C (peak 2) (Fig. 6).

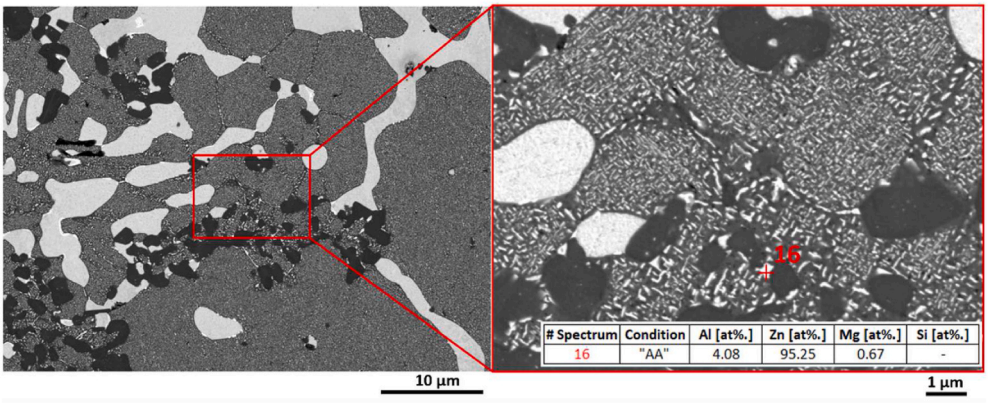

Fig. 10. Micrograph of the specimen in the "AA" (Artificial Aging) condition. In detail, aluminum matrix with precipitated zinc phase.

6. Conclusions

In this study, the $Al_{58}Zn_{28}Mg_6Si_8$ lightweight multicomponent alloy was designed and the effect of heat treatment on the microstructural phases was studied. Based on the results the following conclusions can be drawn:

- Multicomponent alloy with low density were cast in the Al–Zn–Mg–Si system. The $Al_{58}Zn_{28}Mg_6Si_8$ alloy exhibits a density of less than 3.46 g/cm^3 and a Vickers microhardness value of HV 250 in the solubilized state. Additionally, it shows a liquidus temperature of 580 °C and a solidus temperature of 400 °C.
- A solidification scheme based on both CALPHAD calculations and experimental results is proposed. Seven phase transformations were determined, which include the (Si) phase, the eutectic phases of (Al)+(Si) and (Al)+(Mg_2Si), two phases of the Mg–Zn system, ($MgZn_2$) and (Mg_2Zn_{11}), a miscibility gap, and the (Zn) phase.
- The combined use of the CALPHAD methodology and experimental techniques has proven to be an effective approach for both predicting and validating the microstructure in lightweight multicomponent alloys.
- The TEM results confirm that phase decomposition occurred through the mechanism of spinodal decomposition during the solution treatment.

CRediT authorship contribution statement

J.J. Trujillo-Tadeo: Writing – original draft, preparation, Writing – review & editing, Experiments, Investigation, Visualization, Formal analysis, Validation. **Gurutze Arruebarruena:** Writing – Investigation, Review & Editing, Supervision, Project administration, Funding acquisition. **Teresa Guraya:** Experiments, Review & Editing, Project administration, Funding acquisition. **Yoana Bilbao:** Experiments, Writing - Review & Editing. **H.J. Dorantes-Rosales:** Experiments, Writing - Review & Editing. **Iban Vicario:** Visualization, Investigation Review & Editing. **Iñaki Hurtado:** Conceptualization, Writing - Review & Editing, Supervision, Funding acquisition, Project administration, Visualization. All authors have read and agreed to the published version of the manuscript.

Data availability statement

All the data required to reproduce this work is provided in the manuscript.

Declaration of competing interest

The authors declare that they have no known competing financial interests or personal relationships that could have appeared to influence the work reported in this paper.

Acknowledgment

The authors would like to thank the Basque Government for their financial support, encouragement, and guidance through the Elkartek project KK-2020/00047, as well as the chair of the focus group of this project, Dr. Iñaki Hurtado. We also extend our gratitude to the University of the Basque Country (UPV/EHU) for providing access to the X-ray thermodiffraction facilities, specifically Prof. Teresa Guraya, and to the Instituto Politecnico Nacional (IPN/ESIQIE) for providing access to the TEM facilities, specifically Prof. H.J. Dorantes-Rosales.

References

[1] Maulik O, Kumar D, Kumar S, Dewangan SK, Kumar V. Structure and properties of lightweight high entropy alloys: a brief review. Mater Res Express 2018;5:052001. https://doi.org/10.1088/2053-1591/aabbca.
[2] Kumar A, Gupta M. An insight into evolution of light weight high entropy alloys: a review. Metals 2016;6:199. https://doi.org/10.3390/met6090199.
[3] Lu W, Guo W, Wang Z, Li J, An F, Dehm G, et al. Advancing strength and counteracting embrittlement by displacive transformation in heterogeneous high-entropy alloys containing sigma phase. Acta Mater 2023;246:118717. https://doi.org/10.1016/j.actamat.2023.118717.
[4] Miracle DB, Senkov ON. A critical review of high entropy alloys and related concepts. Acta Mater 2017;122:448–511. https://doi.org/10.1016/j.actamat.2016.08.081.
[5] Luan H, Huang L, Kang J, Luo B, Yang X, Li J, et al. Spinodal decomposition and the pseudo-binary decomposition in high-entropy alloys. Acta Mater 2023;248. https://doi.org/10.1016/j.actamat.2023.118775.
[6] Liao YC, Li TH, Tsai PH, Jang JSC, Hsieh KC, Chen CY, et al. Designing novel lightweight, high-strength and high-plasticity Ti (AlCrNb)100- medium-entropy alloys. Intermetallics 2020;117:106673. https://doi.org/10.1016/j.intermet.2019.106673.
[7] Toda-Caraballo I, Rivera-Díaz-del-Castillo PEJ. Modelling solid solution hardening in high entropy alloys. Acta Mater 2015;85:14–23. https://doi.org/10.1016/j.actamat.2014.11.014.
[8] Jahangiri H, Mohagheghi S, Asghari Alamdari A, Yilmaz R, Gürcan Bayrak K, Yu F, et al. Microstructure development and mechanical performance of Al2CrFeMnTi light-weight high entropy alloy. Intermetallics 2021;139:107376. https://doi.org/10.1016/j.intermet.2021.107376.
[9] Zhu C, Xu L, Liu M, Guo M, Wei S. A review on improving mechanical properties of high entropy alloy: interstitial atom doping. J Mater Res Technol 2023;24:7832–51. https://doi.org/10.1016/j.jmrt.2023.05.002.
[10] Xiao WC, Liu SF, Zhao YL, Kai JJ, Liu XJ, Yang T. A novel single-crystal L12-strengthened Co-rich high-entropy alloy with excellent high-temperature strength and antioxidant property. J Mater Res Technol 2023;23:2343–50. https://doi.org/10.1016/j.jmrt.2023.01.182.
[11] Tsai M-H, Tsai R-C, Chang T, Huang W-F. Intermetallic phases in high-entropy alloys: statistical analysis of their prevalence and structural inheritance. Metals 2019;9:247. https://doi.org/10.3390/met9020247.
[12] Heydari H, Tajally M, Habibolahzadeh A. Calculations to introduce some light high entropy alloys based on phase formation rules. J Alloys Compd 2022;912:165222. https://doi.org/10.1016/j.jallcom.2022.165222.
[13] Guo Q, Xu X, Pei X, Duan Z, Liaw PK, Hou H, et al. Predict the phase formation of high-entropy alloys by compositions. J Mater Res Technol 2023;22:3331–9. https://doi.org/10.1016/j.jmrt.2022.12.143.
[14] Wu H, Xie J, Yang H, Shu D, Hou G, Li J, et al. A cost-effective eutectic high entropy alloy with an excellent strength-ductility combination designed by VEC criterion. J Mater Res Technol 2022;19:1759–65. https://doi.org/10.1016/j.jmrt.2022.05.165.
[15] Yin KX, Dong GY, Zhang GJ, Tian QW, Wang YN, Huang JC. Prediction of phase structures of solid solutions for high entropy alloys. J Mater Res Technol 2023;24:7654–65. https://doi.org/10.1016/j.jmrt.2023.04.191.
[16] Zhu W, Huo W, Wang S, Wang X, Ren K, Tan S, et al. Phase formation prediction of high-entropy alloys: a deep learning study. J Mater Res Technol 2022;18:800–9. https://doi.org/10.1016/j.jmrt.2022.01.172.
[17] Gao MC, Yeh J-W, Liaw PK, Zhang Y. High-entropy alloys. Cham: Springer International Publishing; 2016. https://doi.org/10.1007/978-3-319-27013-5.
[18] Feng R, Gao MC, Zhang C, Guo W, Poplawsky JD, Zhang F, et al. Phase stability and transformation in a light-weight high-entropy alloy. Acta Mater 2018;146:280–93. https://doi.org/10.1016/j.actamat.2017.12.061.
[19] Li R, Gao JC, Fan K. Study to microstructure and mechanical properties of Mg containing high entropy alloys. Mater Sci Forum 2010;650:265–71. https://10.4028/www.scientific.net/MSF.650.265.
[20] Chauhan P, Yebaji S, Nadakuduru VN, Shanmugasundaram T. Development of a novel light weight Al35Cr14Mg6Ti35V10 high entropy alloy using mechanical alloying and spark plasma sintering. J Alloys Compd 2020;820:153367. https://doi.org/10.1016/j.jallcom.2019.153367.
[21] Youssef KM, Zaddach AJ, Niu C, Irving DL, Koch CC. A novel low-density, high-hardness, high-entropy alloy with close-packed single-phase nanocrystalline structures. Mater Res Lett 2015;3:95–9. https://doi.org/10.1080/21663831.2014.985855.
[22] Sanchez JM, Vicario I, Albizuri J, Guraya T, Garcia JC. Phase prediction, microstructure and high hardness of novel light-weight high entropy alloys. J Mater Res Technol 2019;8:795–803. https://doi.org/10.1016/j.jmrt.2018.06.010.
[23] Gorsse S, Senkov ON. About the reliability of CALPHAD predictions in multicomponent systems. Entropy 2018;20. https://doi.org/10.3390/e20120899.
[24] Asadikiya M, Zhang Y, Wang L, Apelian D, Zhong Y. Design of ternary high-entropy aluminum alloys (HEAls). J Alloys Compd 2022;891:161836. https://doi.org/10.1016/j.jallcom.2021.161836.

[25] Haga T, Imamura S, Fuse H. Fluidity investigation of pure Al and Al-Si alloys. Materials 2021;14:5372. https://doi.org/10.3390/ma14185372.
[26] Kogo S, Hirosawa S. Thermodynamic assessment and determination of spinodal lines for Al-Zn binary system. Mater Sci Forum 2014;794–796:634–9.
[27] Lopez-Hirata VM, Avila-Davila EO, Saucedo-Muñoz M-L, Villegas-Cardenas JD, Soriano-Vargas O. Analysis of spinodal decomposition in Al-Zn and Al-Zn-Cu alloys using the nonlinear Cahn-Hilliard equation. Mater Res 2017;20:639–45. https://doi.org/10.1590/1980-5373-mr-2015-0373.
[28] Miller MK, Burke MG, Brenner SS. Morphological interpretation of modulated microstructures. J Phys Colloq 1984;45:239–44. https://doi.org/10.1051/jphyscol:1984940.
[29] Edington JW. The operation and calibration of the electron microscope. London: Macmillan Education UK; 1974. https://doi.org/10.1007/978-1-349-02574-9.
[30] Bilbao Y, Trujillo JJ, Vicario I, Arruebarrena G, Hurtado I, Guraya T. X-Ray thermo-diffraction study of the aluminum-based multicomponent alloy Al58Zn28Si8Mg6. Materials 2022;15:5056. https://doi.org/10.3390/ma15145056.
[31] Popovic S, Grèta B. Precipitation and dissolution phenomena in Al-Zn alloys. Croat Chem Acta 1999;72:621–43.